

Crossover from nonadiabatic to adiabatic electron transfer reactions: Multilevel blocking Monte Carlo simulations

L. Mühlbacher¹ and R. Egger²

¹*Fakultät für Physik, Albert-Ludwigs-Universität, D-79104 Freiburg, Germany*

²*Institut für Theoretische Physik, Heinrich-Heine-Universität, D-40225 Düsseldorf, Germany*

(Date: June 11, 2018)

The crossover from nonadiabatic to adiabatic electron transfer has been theoretically studied under a spin-boson model (dissipative two-state system) description. We present numerically exact data for the thermal transfer rate and the time-dependent occupation probabilities in largely unexplored regions of parameter space, using real-time path-integral Monte Carlo simulations. The dynamical sign problem is relieved by employing a variant of the recently proposed multilevel blocking algorithm. We identify the crossover regime between nonadiabatic and adiabatic electron transfer, both in the classical (high-temperature) and the quantum (low-temperature) limit. The electron transfer dynamics displays rich behaviors, including multi-exponential decay and the breakdown of a rate description due to vibrational coherence.

I. INTRODUCTION

Electron transfer (ET) reactions are important for an understanding of many processes in chemistry, biology and physics. Popular examples include charge transfer in semiconductors, chemical reactions, or the primary ET step in bacterial photosynthesis, and, despite the long history of the field [1,2], ET still attracts unbroken and (probably exponentially) increasing attention [3,4]. In this paper, a theoretical study of ET reactions based on the spin-boson (dissipative two-state) description is presented. The spin-boson model provides a well-established description of ET processes in condensed phase environments, which can be motivated from the central limit theorem or, alternatively, using linear response theory [5–7]. In this model, two localized quantum states corresponding to the redox sites are taken. This two-level system (TLS) is fully specified by a tunnel splitting $\hbar\Delta$ (which is twice the electronic coupling between the two redox sites), and by a bias $\hbar\epsilon$ (which corresponds to the energy difference between the sites). Of crucial importance is then the coupling to the “environmental” modes (bath), which is modeled as an infinite set of harmonic oscillators with a suitable (continuous) spectral density $J(\omega)$ describing their frequency-resolved coupling strength to the electron. For a given ET system, one can use classical Molecular Dynamics simulations to find the appropriate $J(\omega)$ [5], but below we shall consider a specific class of spectral densities that describes many ET processes quite accurately. Two important parameters following from a given spectral density are the *reorganization energy* $\hbar\Lambda$ (which describes the overall coupling strength) and the typical bath frequency ω_c corresponding to a maximum in $J(\omega)$. This model has been studied in depth in the field of dissipative quantum mechanics [7–11], mostly in the so-called scaling limit for Ohmic spectral densities (see below), but its application to ET reactions is mainly located in a different parameter regime.

Certain limiting cases of ET theory are rather well understood. The primary object of interest is the *thermal rate constant* k_{th} , which is useful if ET dynamics is correctly described by exponential decay. First, for very small Δ , one can use perturbation theory in Δ to obtain the celebrated golden rule rate [12–15]. This is the *nonadiabatic limit*. In the opposite limit of large Δ , the *adiabatic limit*, it is more useful to think in terms of adia-

batic free energy surfaces formed by linear superpositions of the two localized free energies. In that case, the bath essentially is very slow (“classical”) compared to the electronic motion, and one can develop a simple theoretical description again [16–18]. Notably, the ET dynamics in this regime is often not simply an exponential relaxation but exhibits oscillatory or multi-exponential behavior at low temperatures [19,20]. At sufficiently high temperatures, the famous *classical Marcus theory* [1,2], or semiclassical generalizations thereof [3], apply. For a path-integral approach to Marcus theory, see also Ref. [21]. Marcus theory also makes predictions about the rate constant in the crossover regime between nonadiabatic and adiabatic ET. It should be stressed that the spin-boson model contains all these results as limiting cases in the full parameter space.

Notably, the spin-boson problem cannot be solved analytically without imposing approximations. One important exception to this rule is the case of an Ohmic spectral density, see Eq. (17) below, with the restrictions:

$$\Delta/\omega_c \ll 1, \quad k_B T/\hbar\omega_c \ll 1 \quad \Leftrightarrow \quad \text{scaling limit.} \quad (1)$$

In this scaling limit, sophisticated conformal field theory techniques are able to yield the complete non-equilibrium solution for the dynamics under arbitrary initial preparation [22]. Besides this solution, whose parameter regime is of little interest to ET theory, if one is interested in analytical progress, one has several options for approximations. One possibility is to work perturbatively in the tunnel splitting Δ . This leads to the noninteracting blip approximation (NIBA) [23–25], which is basically equivalent to the golden rule formula for the rate constant. Other approaches are based on variational treatments [26] or work perturbatively in the system-bath coupling (Redfield approach) [27]. As typical reorganization energies are quite sizeable, a perhaps more promising route is to use the powerful computer simulation methods available by now.

Let us then briefly summarize the numerical methods that have been applied to a study of the spin-boson dynamics. An approximate approach which has become quite popular recently employs a mixed quantum/classical (or quantum/semiclassical) description [28–37]. However, such studies are typically restricted to a few bath modes. Unless one has a situation with only a few strongly coupled bath modes, the more typical situation of condensed-phase ET reactions is difficult to describe using such methods. In addition, it is hard to estimate the errors made under these approximations. Similar arguments apply to time-dependent Hartree methods (basis set approach) [38] and to memory-equation approaches [39,40]. The latter method, as well as the recently proposed stochastic Langevin-type simulation [41,42], dynamical Wilson renormalization group [43,44] and the real-time renormalization group [45], basically appear to be restricted

to the Markovian limit realized for an Ohmic bath with $\omega_c \rightarrow \infty$, yet most situations of interest for ET are located outside the Markovian regime. The methods discussed so far are therefore very powerful in certain parameter regions of the spin-boson model (in fact much more powerful than our method employed below), but may fail badly in others.

A method free from such restrictions is provided by *Monte Carlo simulations* [46], in particular the powerful path-integral Monte Carlo (PIMC) approach. In principle, this approach is numerically exact throughout the full parameter space, i.e. for arbitrary spectral density, tunnel coupling, temperature and/or bias. However, as one is really interested in the ET *dynamics* in real time, a direct application of quantum Monte Carlo (QMC) methods is plagued by the infamous *sign problem* [47]. One alternative is to carry out an imaginary-time simulation, which is intrinsically free of the sign problem, and then analytically continue the data to real time. This program has been carried out for the spin-boson problem, either using Pade approximants [48,49] or Maximum Entropy methods [50] in order to perform the analytical continuation. The latter procedure is mathematically ill-defined and quite troublesome to carry out. In addition, by using this procedure, one is inevitably restricted to equilibrium situations. However, in ET reactions one often has a true non-equilibrium preparation, e.g. one photoexcites an electron to the donor state at time $t = 0$ and then follows the time evolution of the occupation probability. Such a question has to be answered by a true non-equilibrium real-time calculation.

Such a calculation is presented in our study. The price to pay for working in real time and still keeping exactness and applicability throughout the full parameter space is however quite high. The main challenge is due to the sign problem, which implies that one is restricted in the real-time range up to which stable calculations can be done. The sign problem arises from the destructive interference of a large number of quantum paths at long times, leading to a very small signal-to-noise ratio and thus rendering the simulations numerically unstable. Early real-time PIMC attempts for computing the spin-boson dynamics [51–53] were based on the stationary-phase Monte Carlo approach [54–56] or variations thereof. Such filtering methods try to keep the MC trajectory close to the important stationary-phase regions of path space. While this is able to somewhat relieve the sign problem, a more powerful method is available by now. This “multilevel blocking” (MLB) algorithm [57–60] has been proposed and successfully used to relieve both the fermionic and the dynamical sign problem. MLB represents a systematic recursive implementation of a simple *blocking strategy*. Roughly speaking, the blocking strategy is equivalent to a naive filtering, and one can think of MLB as a systematic and optimized way of implementing the filtering idea. Here we shall employ a recently proposed MLB

variant which can account for effective actions [59] of the type encountered in PIMC for the spin-boson model. This approach is superior to previous real-time PIMC methods, and allows to compute the spin-boson dynamics up to timescales of practical interest *without approximations and for the full parameter regime relevant to ET reactions*.

The remainder of this paper is as follows. In Sec. II we briefly describe the spin-boson model and the dynamical quantities of interest. Next we describe our QMC method, see Sec. III. Since the method has been exposed in great detail in Ref. [59], focusing on exactly the same model, we largely refrain from repeating ourselves here. Technical details of interest to experts are given in the Appendix. In Section IV we then present our numerical results for the dynamical quantities and the rate k_{th} for various regimes, including the important crossover region between nonadiabatic and adiabatic ET. The most difficult regime is at low temperatures, a regime that can now be treated by PIMC. In presenting the numerical results, we restrict ourselves to the symmetric (unbiased) case $\epsilon = 0$, leaving the biased system for future studies. Finally, some conclusions are drawn in Sec. V.

II. ELECTRON TRANSFER THEORY

The spin-boson model (dissipative two-state system) is defined by the Hamiltonian [7]

$$H = H_0 + H_I + H_B = -\frac{\hbar\Delta}{2}\sigma_x + \frac{\hbar\epsilon}{2}\sigma_z - \sigma_z \sum_{\alpha} C_{\alpha} X_{\alpha} + \sum_{\alpha} \left(\frac{P_{\alpha}^2}{2m_{\alpha}} + \frac{1}{2} m_{\alpha} \omega_{\alpha}^2 X_{\alpha}^2 \right), \quad (2)$$

where the free TLS is described by H_0 , containing the tunnel splitting $\hbar\Delta$ and the energy gap $\hbar\epsilon$ between the two localized electronic states. Here σ_x and σ_z denote the standard Pauli matrices acting in TLS space, where the $|+\rangle$ ($|-\rangle$) state refers to the donor (acceptor). The environmental modes are modeled by an infinite collection of harmonic oscillators, H_B , which bilinearly couple to the position of the electron (H_I). For the great majority of ET systems, this model provides a reasonably accurate description of reality, as is discussed and motivated at length in Refs. [5–7,15]. Within this model, the bath parameters affect ET only via the spectral density

$$J(\omega) = \frac{2\pi}{\hbar} \sum_{\alpha} \frac{C_{\alpha}^2}{m_{\alpha}\omega_{\alpha}} \delta(\omega - \omega_{\alpha}), \quad (3)$$

which effectively becomes a continuous function of ω for a condensed-phase environment and determines all bath correlation functions that are relevant for the ET dynamics. For instance, the complex-valued bath autocorrelation function for complex time $z = t - i\tau$ is for $\beta = 1/k_B T$ given by

$$L(z) = \int_0^{\infty} \frac{d\omega}{\pi} J(\omega) \frac{\cosh[\omega(\hbar\beta/2 - iz)]}{\sinh(\hbar\beta\omega/2)}. \quad (4)$$

Similarly, the important *reorganization energy* $\hbar\Lambda$ of Marcus theory [1,2] is defined by

$$\Lambda = \int_0^{\infty} d\omega \frac{J(\omega)}{\pi\omega}, \quad (5)$$

which is the only important bath quantity in the classical (high-temperature) limit, as is apparent from classical Marcus theory. Details of $J(\omega)$ matter only at low temperatures.

In the following we focus on the two dynamical properties of primary relevance to ET dynamics. The *time-dependent occupation probability* is defined as

$$P(t) = \langle \sigma_z(t) \rangle = \langle e^{iHt/\hbar} \sigma_z e^{-iHt/\hbar} \rangle \quad (6)$$

and gives the difference in the occupation probabilities of the donor and the acceptor state with the electron initially held fixed on the donor. This quantity then directly probes ET dynamics after the non-equilibrium initial preparation corresponding to the initial density matrix

$$W(0) = |+\rangle\langle +| e^{-\beta(H_B + \mu\mathcal{E})}. \quad (7)$$

Here μ is the dipole moment of the electron, and \mathcal{E} denotes the dynamical polarization of the bath [7], with the electron in the donor state and the bath equilibrated with respect to it. By comparing with Eq. (2), we see that $\mu\mathcal{E} = -\sum_{\alpha} C_{\alpha} X_{\alpha}$. As pointed out in Ref. [33], this “standard preparation” often used in ET experiments is unfavorable for coherent (oscillatory) dynamics when compared to other initial preparations. Therefore it is especially suitable for a thermal transfer rate description.

In addition, we calculate the complex-valued *correlation function*

$$C(t) = \langle \sigma_z(0) \sigma_z(t) \rangle_{\beta} = Z^{-1} \text{tr} \left\{ e^{-\beta H} \sigma_z e^{iHt/\hbar} \sigma_z e^{-iHt/\hbar} \right\} \quad (8)$$

with $Z = \text{tr} \exp(-\beta H)$. This quantity probes the dynamics under an equilibrium preparation and, for $\epsilon = 0$, differs from $P(t)$ only through the initial preparation. At high temperatures, one generally expects that initial preparation effects show little influence on the dynamics, and therefore a unique rate constant k_{th} should exist. The inverse rate would then be the timescale governing the relaxation of both $P(t)$ and $C(t)$. However, in the quantum regime one needs to be more careful, and the specific experiment under study will determine which is the relevant dynamical quantity.

Assuming for the moment that there is a unique rate constant k_{th} , $P(t)$ should follow a simple exponential decay for times t large compared to some transient molecular timescale τ_{trans} of the order $1/\omega_c$, yet small compared

to the relaxation timescale $\tau_{\text{relax}} \approx 1/k_{th}$. Calculating $P(t)$ for $\tau_{\text{trans}} \ll t \ll \tau_{\text{relax}}$ would then allow to extract the temperature-dependent thermal transfer rate. The thermal transfer rate (if it exists) can also be obtained via a *time-dependent function* defined under an equilibrium preparation [10],

$$k_f(t) = \frac{2}{\hbar\beta Z_A} \text{Im tr} [e^{-\beta H} h_A(0) h_A(t)], \quad (9)$$

where $h_A = |+\rangle\langle+| = (1 + \sigma_z)/2$ denotes a projector onto the donor state and $Z_A = \text{tr}\{e^{-\beta H} h_A\}$ its partition sum. The thermal rate constant then follows from Eq. (9) as the *plateau value* for times t where $k_f(t)$ forms a plateau. According to our above discussion, this should happen for $\tau_{\text{trans}} \ll t_{\text{pl}} \ll \tau_{\text{relax}}$ where $t = t_{\text{pl}}$ is a suitable plateau time. The index f in Eq. (9) denotes a *forward rate*, describing the directed transfer rate from the donor to the acceptor site. The total rate k_{th} probed by $P(t)$ is the sum of the forward and the backward rate k_f and k_b , which in turn are connected via a standard detailed-balance relation,

$$k_b(T, \epsilon) = k_f(T, \epsilon) \exp(-\hbar\epsilon/k_B T). \quad (10)$$

Notably, if τ_{trans} and τ_{relax} are not well separated, no transfer rate can be defined, and a simple rate formalism breaks down. Such a breakdown of the rate description could happen, for instance, for very fast reactions. Equation (9) thus not only yields a convenient way to compute the thermal transfer rate, but also a means to decide upon the validity of the rate picture of ET at all. It is important to stress that $k_f(t)$ does not refer to a time-dependent rate reflecting the dynamics of $P(t)$ but is only an auxiliary function allowing to determine the time-independent rate k_{th} when it exists. Equation (9) can be expressed in terms of $C(t)$,

$$k_f(t) = \frac{1}{\hbar\beta} \frac{\text{Im } C(t)}{1 + \langle\sigma_z\rangle_\beta}, \quad (11)$$

with $\langle\sigma_z\rangle_\beta = Z^{-1} \text{tr}\{e^{-\beta H} \sigma_z\}$. The fact that $P(t)$ will follow an exponential decay only after some time τ_{trans} is made explicit by noting that $dP/dt(t=0) = 0$ due to $d\sigma_z(t)/dt \sim \sigma_y(t)$. Our main goal is therefore to calculate the ET dynamics up to real times that are significantly larger than τ_{trans} .

Before turning to the numerical computations, let us briefly summarize some simple limiting cases, where analytical results are available. In the *nonadiabatic limit*, Eq. (9) can be evaluated for arbitrary temperatures using Fermi's golden rule,

$$k_f^{GR} = \frac{\Delta^2}{4} \int_{-\infty}^{\infty} dt \exp[i\epsilon t - Q(t)], \quad (12)$$

with the twice-integrated bath autocorrelation function:

$$d^2 Q(z)/dz^2 = L(z) \quad \text{with} \quad Q(0) = 0. \quad (13)$$

For special choices of $J(\omega)$, it is possible to evaluate the remaining integral explicitly [15]. In the *adiabatic limit*, the bath is very slow and thus behaves classically. Essentially, it then represents a static random field obeying Gaussian statistics, which acts as an additional fluctuating energy gap between the electronic states. The ET dynamics then follows from the free TLS dynamics by including a fluctuating bias [5]. The inevitable failure of this approach at long times can in principle be relieved by applying appropriate Bloch-type equations [16]. Third, for high temperatures, *classical Marcus theory* [2] can be recovered from the spin-boson description [21] and predicts the forward rate

$$k_f^{cl} = \frac{\Delta^2}{4 + \pi\Delta^2/(\Lambda\omega_r)} \sqrt{\frac{\pi\hbar}{\Lambda k_B T}} e^{-F^*(\epsilon)/k_B T}, \quad (14)$$

with the activation free energy barrier given by the celebrated *Marcus parabola*,

$$F^*(\epsilon) = \hbar(\epsilon - \Lambda)^2/4\Lambda, \quad (15)$$

and a solvent frequency scale ω_r . For the Ohmic spectral density (17), this frequency was computed approximately in Ref. [21], with the result

$$\omega_r \approx \frac{\omega_c}{2}. \quad (16)$$

Marcus theory yields a classical rate constant covering the full crossover from nonadiabatic to adiabatic ET. Equation (14) coincides with the high-temperature limits of the nonadiabatic rate (12) and of the adiabatic formulation for $\Delta \ll \omega_c$ and $\Delta \gg \omega_c$, respectively. In the adiabatic limit, the rate is independent of Δ . From Eq. (14), the crossover regime is expected for $\Delta/\omega_c \approx \sqrt{\Lambda/\omega_c}$, at least for high temperatures.

In all simulations reported in this paper, we consider an *Ohmic spectral density* with exponential cutoff [7],

$$J(\omega) = 2\pi\alpha\omega e^{-\omega/\omega_c}, \quad (17)$$

with dimensionless damping strength α and a cutoff frequency ω_c . For many polar solvents, it is appropriate to choose ω_c according to some intermediate bath frequency [15]. Instead of α , it is often more convenient to measure the coupling strength to the bath in terms of the reorganization energy (5). For this spectral density, one finds $\Lambda = 2\alpha\omega_c$. In addition, the correlation function (13) can be given in closed form [15],

$$Q(z) = 2\alpha \left[\ln(1 + i\omega_c z) - \ln \left(\frac{\Gamma(\Omega + iz/\hbar\beta)\Gamma(\Omega - iz/\hbar\beta)}{\Gamma^2(\Omega)} \right) \right], \quad (18)$$

with the gamma function $\Gamma(z)$ and the abbreviation

$$\Omega = 1 + k_B T / \hbar \omega_c. \quad (19)$$

Note that the second contribution in $Q(z)$ in Eq. (18) vanishes for $T = 0$.

Let us also summarize at this point some of the analytically known results for this class of spectral densities. First, the complete temperature dependence of the nonadiabatic golden rule rate (12) is known for $\alpha = 1/2$ and $\alpha = 1$. For $\epsilon = 0$, the result is [15]

$$k_f^{GR}(\alpha = 1/2) = \frac{\pi \Delta^2 \Gamma(2\Omega - 1)}{\omega_c 2^{2\Omega} \Gamma^2(\Omega)}, \quad (20)$$

$$k_f^{GR}(\alpha = 1) = \frac{\pi \Delta^2 \Gamma^4(2\Omega - 1)}{2 \hbar \beta \omega_c^2 \Gamma^4(\Omega) \Gamma(4\Omega - 2)}. \quad (21)$$

Second, the complete dynamics for $\alpha = 1/2$ in the scaling limit defined by Eq. (1) is known. For instance, the quantity $P(t)$ obeys a simple exponential relaxation for $\epsilon = 0$ and $\omega_c t \gg 1$,

$$P(t) = \exp\left(-\frac{\pi \Delta^2}{2\omega_c} t\right), \quad (22)$$

where the relaxation rate is twice the low-temperature limit of Eq. (20). Notably, for $\alpha \neq 1/2$ but close to $1/2$, the dynamics is much more complicated, with algebraic decay and oscillatory behaviors [7]. These features are due to *electronic coherence* effects, which one generally does not expect to survive in ET reactions. This is also reflected in the behavior of $C(t)$ for $\alpha = 1/2$, which exhibits long-time algebraic tails. Therefore one cannot expect that the time-dependent function $k_f(t)$ will exhibit plateau behavior, although it is possible to define a rate for the decay of $P(t)$. This reflects the importance of the initial preparation in that case.

III. SIMULATION METHOD

Next we turn to a computational method able to yield the rate constant. A great simplification arises due to the harmonic nature of the bath and the bilinear coupling in Eq. (2), which allows to perform the trace over the bath degrees of freedom in Eqs. (6) and (8) in an *exact* manner. Adopting a path-integral approach, one obtains, e.g. for $C(t)$ [7],

$$C(t) = Z^{-1} \int \mathcal{D}\sigma \sigma(0) \sigma(t) \exp\left\{\frac{i}{\hbar} S_0[\sigma] - \Phi[\sigma]\right\}. \quad (23)$$

Here the path integration runs over paths $\sigma(z)$ for the discrete ‘‘spin’’ variable $\sigma = \pm 1$ corresponding to σ_z , with the complex time z following the Kadanoff-Baym contour γ depicted in Fig. 1. Furthermore, $S_0[\sigma]$ denotes the total action of the free TLS, and the influence of the

traced-out bath is encoded in the *influence functional* $\Phi[\sigma]$. In terms of the bath autocorrelation function (4), it reads [7]

$$\Phi[\sigma] = \frac{1}{4} \int_{\gamma} dz \int_{z' < z} dz' \sigma(z) L(z - z') \sigma(z'), \quad (24)$$

where time integrations are ordered along the contour γ . The influence functional introduces long-ranged interactions along the real and imaginary time axes, rendering the evaluation of the remaining path integral in Eq. (23) a difficult task.

Quantum-mechanical expectation values like Eq. (23) can be calculated in a numerically exact way by PIMC simulations. To make Eq. (23) accessible to PIMC, the path integral is taken in its discretized form with N discretization steps. Following the scheme described in Refs. [53,59], q uniformly spaced points are used for each of the real-time paths $z : 0 \rightarrow t$ and $z : t \rightarrow 0$, and r points for the imaginary-time path $z : 0 \rightarrow -i\hbar\beta$, with discretization steps

$$\Delta_j = \begin{cases} t/q, & 1 \leq j \leq q \\ -t/q, & q+1 \leq j \leq 2q \\ -i\hbar\beta/r, & 2q+1 \leq j \leq 2q+r, \end{cases} \quad (25)$$

leading to $N = 2q + r$ discrete time points $z_i = \sum_{j=1}^{i-1} \Delta_j$. Using $\sigma_i = \sigma(z_i) = \pm 1$, Eq. (23) can be written as

$$C(t) = Z^{-1} \sum_{\{\sigma_j\}} \sigma_1 \sigma_{q+1} \rho[\{\sigma_j\}],$$

$$\rho[\{\sigma_j\}] = \left[\prod_{i=1}^N K(\sigma_i, \sigma_{i+1}) \right] e^{-\Phi[\{\sigma_j\}]} \quad (26)$$

with $Z = \sum_{\{\sigma_j\}} \rho[\{\sigma_j\}]$ and $\sigma_{N+1} = \sigma_1$ due to the cyclic nature of the trace. The sum runs over all realizations of the discretized spin path $\{\sigma_j\} = \{\sigma_1, \dots, \sigma_N\}$, and

$$K(\sigma_i, \sigma_{i+1}) = \langle \sigma_{i+1} | \exp(-i\Delta_i H_0 / \hbar) | \sigma_i \rangle \quad (27)$$

denotes the short-time propagator of the free TLS, which is a known 2×2 matrix. Note that due to $\langle \sigma(0) \sigma(t) \rangle_{\beta} = \langle \sigma(t') \sigma(t' + t) \rangle_{\beta}$, one single MC trajectory can be used to compute $C(t_1)$ for all times $t_1 \leq t$. Furthermore, exploiting $\langle \sigma(0) \sigma(t_k) \rangle_{\beta} = \langle \sigma(t_k) \sigma(0) \rangle_{\beta}^*$ in a similar way improves the MC statistics. A discretized version of the influence functional is given by

$$\Phi[\{\sigma_j\}] = \frac{1}{8} \sum_{j,k=1}^N \sigma_j L_{jk} \sigma_k, \quad (28)$$

with the complex-valued influence matrix [53]

$$L_{jk} = L_{kj} = Q(z_j - z_k + (\Delta_j + \Delta_{k-1})/2) \\ + Q(z_j - z_k + (-\Delta_{j-1} - \Delta_k)/2) \\ - Q(z_j - z_k + (-\Delta_{j-1} + \Delta_{k+1})/2) \\ - Q(z_j - z_k + (\Delta_j - \Delta_k)/2) \quad \text{for } j > k, \\ L_{jj} = 2Q((\Delta_{j-1} + \Delta_j)/2), \quad (29)$$

where $Q(z)$ is given in Eq. (13). To make further progress, and also to correct a misprint in Ref. [53], we now denote the spins σ_{2q+2-j} for $1 \leq j \leq q+1$ (residing on the backward real-time branch of γ) by σ'_j , and, similarly, the imaginary-time spins σ_{2q+m} for $2 \leq m \leq r$ by $\bar{\sigma}_m$. In the next step, employ the coordinate transformation

$$\eta_j = \frac{1}{2}(\sigma_j + \sigma'_j), \quad \xi_j = \frac{1}{2}(\sigma_j - \sigma'_j).$$

These are ‘‘classical’’ and ‘‘quantum’’ variables for electronic motion [53]. Exploiting the symmetry relations $Q(z - i\hbar\beta) = Q(-z)$ and $Q(z^*) = Q^*(-z)$, one finally arrives at

$$\begin{aligned} \Phi[\{\bar{\sigma}_m, \eta_j, \xi_j\}] &= \sum_{m>n=2}^r \bar{\sigma}_m Y_{mn} \bar{\sigma}_n - \frac{1}{4} \sum_{j=1}^q \sigma_j \sigma'_j \Lambda_{jj} \\ &+ \sum_{j>k=1}^q \xi_j (\Lambda_{jk} \xi_k + iX_{jk} \eta_k) + \sum_{j=1}^q \sum_{m=2}^r \xi_j Z_{jm} \bar{\sigma}_m \\ &+ \frac{\sigma'_1}{4} \sum_{m=2}^r \bar{\sigma}_m (L_{2q+m,1} + L_{2q+m,2q+1}), \end{aligned} \quad (30)$$

with the matrices

$$\begin{aligned} Y_{mn} &= \frac{1}{4} L_{2q+m,2q+n}, & \Lambda_{jk} &= \text{Re } L_{jk}, \\ X_{jk} &= \text{Im } L_{jk}, & Z_{jm} &= \frac{1}{2} L_{j,2q+m} \end{aligned}$$

where $1 \leq j, k \leq q$ and $2 \leq m, n \leq r$. Equation (30) together with the contribution from the TLS propagator (27) constitutes a discretized form of the total action which is useful for PIMC simulations. Finally, to obtain $P(t)$ instead of $C(t)$, the imaginary-time spin contributions in Eq. (30) and in the free propagator have to be neglected, with $\sigma_1 = \sigma'_1 = +1$ reflecting the initial non-equilibrium preparation. Instead of sampling an entirely new MC trajectory according to this new weight, $P(t)$ can also be calculated from the same MC trajectory as $C(t)$ by including a correction factor which accommodates the changes in the corresponding MC weight. We refer the interested reader to the Appendix for computational details. Although the latter approach exhibits poorer statistics, it still produces satisfying results in most cases. We therefore use it for the simultaneous calculation of $k_f(t)$ and $P(t)$, without significant increase in computing time.

Unfortunately, this method suffers from the notorious sign problem. It stems from interference due the complex phase factors assigned to different spin paths $\{\sigma_j\}$, resulting in a small signal-to-noise ratio of the stochastic averaging procedure. The exponential increase of interfering paths with system size N is reflected in an exponential decrease of the signal-to-noise ratio with the maximum real time under study. Here we employ the

multilevel (MLB) approach in a version suitable to deal with long-ranged interactions along the (complex) time contour, which is capable of relieving the sign problem without introducing approximations. The algorithm is described in detail in Ref. [59], and we only give the basic idea in the following paragraph. For the expert reader, some improvements over Ref. [59] are summarized in the Appendix.

In short, the MLB algorithm is based on the simple observation that the sign problem can be considerably reduced by sampling *blocks* instead of single paths. A block is here built from a small set of paths. Provided the blocks are chosen small enough, stochastic averages within a block do not suffer from the sign problem. Sampling blocks instead of single paths can in fact be shown to always result in a better signal-to-noise ratio [56]. Repeating this scheme iteratively by establishing a hierarchy (‘‘levels’’) of blocks, the exponential severity of the sign problem with respect to the maximum real time t can be changed into an only algebraic one [57–60].

Single spin flips and, on the real-time axis, double spin flips, with simultaneous flips of the forward and backward spins σ_i and σ'_i , were used to propagate the MC trajectory. Furthermore, since the creation of short blips (connected real-time intervals where $\xi_i = 0$) is often energetically more expensive than the creation of more extended ones, we also included flips of complete blocks of subsequent spins to ensure ergodicity. When working with MLB, these blocks must not extend over the borderline separating different levels. However, since the results do not deviate from those obtained with local spin flips alone, we conclude that ergodicity poses no problem for our approach.

IV. NUMERICAL RESULTS

In this section, we present numerical results for the thermal transfer rate k_{th} and the occupation probability $P(t)$ of an unbiased system, $\epsilon = 0$. Of course, then k_{th} is just twice the forward rate k_f . Accordingly, k_{th} was extracted from the plateau value of

$$k(t) = 2k_f(t). \quad (31)$$

Furthermore, the right-hand side of Eq. (11) reduces to $\text{Im}\{C(t)\}/\hbar\beta$ since $\langle\sigma_z\rangle_\beta$ vanishes for $\epsilon = 0$. Our code was carefully tested for (a) $\alpha = 0$ (free TLS), (b) $\alpha = 1/2$ within the scaling limit (1), and (c) for $\alpha = 5$, $\omega_c = 0.5\Delta$, $T = 2\hbar\Delta/k_B$. The numerical results accurately reproduce the available analytical solutions [for (a) and (b)] and the numerical results of Ref. [37] in case (c). For more tests, see Sec. IV A.

We are then interested in mapping out the ET dynamics *phase diagram*, which is a function of three parameters. These are (1) the temperature T , (2) the reorganization energy Λ , where for the bath spectral density

(17) one has $\Lambda = 2\alpha\omega_c$ with a damping parameter α and a cutoff (dominant) frequency ω_c , and (3) the adiabaticity parameter Δ/ω_c with the tunnel splitting Δ . We shall systematically tune these parameters in order to explore the crossover from nonadiabatic to adiabatic ET. To keep the relevant parameter space manageable, we restrict ourselves to the reorganization energy $\Lambda = 10\Delta$, but also give some results for $\Lambda = 50\Delta$ [61]. Unless noted otherwise, below $\Lambda = 10\Delta$ has been taken. We are then left with only two free parameters, namely temperature and the adiabaticity Δ/ω_c . By systematically increasing the latter, one can go from the nonadiabatic into the adiabatic region of the phase diagram. Of course, we use the term “phase diagram” not in the sense of distinct regions separated by phase transitions. Nevertheless, there are regimes where ET dynamics proceeds qualitatively different, which are separated by a rather sharp crossover.

The thermal transfer rate was numerically obtained in two different ways. If $k(t)$ showed a plateau for some plateau time $t_{\text{pl}} > \tau_{\text{trans}}$, the thermal transfer rate k_{th} was taken as the plateau value $k(t_{\text{pl}})$. A second and distinct possibility is to fit $P(t)$ to an exponential decay $\sim \exp(-k_{th}t)$ after the initial transient, $t > \tau_{\text{trans}}$. In fact, we will encounter examples where a rate from $k(t)$ does apparently not exist, or at least requires a modified extraction procedure, while $P(t)$ still displays a well-defined exponential decay on the timescale under study.

A. Special cases

To make contact to analytical theory, let us first describe results for the special damping strengths $\alpha = 1/2$ and $\alpha = 1$. This provides also another check for the numerical MLB-PIMC scheme. In addition, from our data for $\alpha = 1/2$, we can give fairly accurate estimates for the validity of the scaling regime, namely

$$\omega_c/\Delta \gtrsim 6 \quad \hbar\omega_c/k_B T \gtrsim 50. \quad (32)$$

Let us start with $\alpha = 1/2$ and $\omega_c = 50\Delta$, corresponding to the large reorganization energy $\Lambda = 50\Delta$. Here an almost strict exponential decay of $P(t)$ was found at all temperatures, with the rate nicely matching the analytical prediction (20), see Fig. 2. This agreement is of course not surprising since ω_c is much larger than Δ . For $P(t)$, transient short-time dynamics reflecting $dP/dt(0) = 0$ takes place on a significantly shorter timescale than for $k(t)$, where t_{pl} increases for lower temperatures. For $T \lesssim \hbar\Delta/k_B$, $k(t)$ fails to exhibit a plateau while $P(t)$ still allows for a useful rate description. This shows the increasing significance of electronic coherence in this parameter regime [7].

This point becomes even more obvious for $\Lambda = 10\Delta$, where $\Delta/\omega_c = 0.1$. Now $k(t)$ fails to exhibit a plateau at all temperatures studied, $0.2 \leq k_B T/\hbar\Delta \leq 10$. However, the rate obtained from $P(t)$ still closely follows

the nonadiabatic prediction (20), see Fig. 2. In addition, for $\alpha = 1/2$ and $T = \hbar\Delta/k_B$, the dependence on the adiabaticity parameter was studied within the range $10 \leq \omega_c/\Delta \leq 100$. Again the nonadiabatic prediction is nicely reproduced, proving its usefulness in this regime, see Fig. 3. The excellent agreement of Eq. (20) with our results allows for the quantitative identification of the scaling regime. The rate (20) reaches the scaling value $\pi\Delta^2/2\omega_c$ within a relative error of r %, if

$$\frac{\hbar\omega_c}{k_B T} = \frac{423}{r}. \quad (33)$$

Our data indicate that this criterion also holds for the numerically exact ET rate for (at least) $0.1 \leq r \leq 10$, $0.01 \leq \Delta/\omega_c \leq 0.2$, and $0.05 \leq k_B T/\hbar\Delta \leq 20$. Note that this also agrees with Eq. (32) for $r \approx 8.5$ %.

The second special case, to which we now turn, is defined by $\alpha = 1$. Again starting with $\Lambda = 50\Delta$, the obtained rate closely follows the nonadiabatic prediction (21) for all temperatures investigated, $0.2 \leq k_B T/\hbar\Delta \leq 20$, see Fig. 4, whereas the classical (high-temperature) Marcus rate (14) fails to give an accurate picture except for $T \geq 40\hbar\Delta/k_B = 1.6\hbar\omega_c/k_B$. The absence of electronic coherence and the nice separation of transient and relaxation timescales is reflected in the fact that $k(t)$ reaches a plateau within the whole temperature range. The corresponding thermal rate constant is identical to the rate extracted from the exponential decay of $P(t > \tau_{\text{trans}})$. Moreover, in contrast to $\alpha = 1/2$, this exponential decay is preceded by a steep decrease of the population for $T \leq 5\hbar\Delta/k_B$ on timescales $t \lesssim \tau_{\text{trans}} \simeq 0.5\Delta^{-1}$. The timescale τ_{trans} (approximately) coincides for both $P(t)$ and $k(t)$, see Fig. 5, and remains fairly constant with temperature. The $\alpha = 1$ rate for given other parameters is smaller than for $\alpha = 1/2$. Since with our conventions, $\alpha = 1/2$ corresponds to a “more nonadiabatic” regime, this finding is not surprising. Recrossing events, which are irrelevant in the nonadiabatic limit, will generally decrease the rate.

For $\Lambda = 10\Delta$, we find a similar scenario, with the Marcus rate failing except for $T \geq 10\hbar\Delta/k_B = 2\hbar\omega_c/k_B$. However, $k(t)$ does not exhibit a plateau, since ET dynamics is now very fast and hence $\tau_{\text{trans}} \ll \tau_{\text{relax}}$ does not hold anymore. Remarkably, $P(t > \tau_{\text{trans}})$ still shows exponential decay with the nonadiabatic rate (21), see Fig. 4. Note that here the adiabaticity parameter is already as large as $\Delta/\omega_c = 0.2$.

B. Crossover regime

Entering the crossover regime between nonadiabatic and adiabatic ET (taking $\Lambda = 10\Delta$), let us start with $\Delta/\omega_c = 1$. In this case, the extraction of the thermal transfer rate from $k(t)$ fails for high temperatures,

$T \gtrsim 2\hbar\Delta/k_B$. After an initial peak, $k(t)$ decreases almost linearly instead of exhibiting a plateau. The high-temperature absence of a plateau may be rationalized by noting that the classical activation barrier (15) corresponds to $T = 2.5\hbar\Delta/k_B$. For higher temperatures, ET is practically activationless, so that transient and relaxation timescale are not really separated anymore. However, after a rapid initial transient decay, $P(t > \tau_{\text{trans}})$ decays exponentially with the rate k_{th} . Interestingly, this rate coincides with the value of $k(t)$ at the transition from the initial peak to the linear decrease, see Fig. 6, and governs the behavior of $P(t)$ for $\tau_{\text{trans}} \lesssim t \lesssim \tau_{\text{trans}} + 0.5k_{th}^{-1}$ (note the increase of the relevant time interval for low temperatures.) The temperature dependence of k_{th} is well described by the Marcus formula (14), see Fig. 7. While the Marcus rate together with Eq. (16) yields a quite accurate description, the nonadiabatic rate (12) overestimates the true rate by a factor ≈ 1.2 . However, overall features (like the temperature at which the maximum of the rate occurs) are still reproduced. This overestimate of the rate can be rationalized in terms of recrossing events between acceptor and donor, which are higher-order contributions in Δ .

For low temperatures, $T \lesssim 0.2\hbar\Delta/k_B$, we have encountered a rather interesting and apparently quite general phenomenon regarding the ET dynamics in the crossover regime. In fact, in this low-temperature crossover regime between nonadiabatic and adiabatic ET, the thermodynamic rate becomes so small that almost no change in $P(t > \tau_{\text{trans}})$ is observed anymore. At the same time, the initial decay of $P(t)$ is ended by a local minimum deepening with decreasing temperature, see Fig. 8. Therefore the relevant ET dynamics solely happens during the initial (transient) stage, which lasts for a few Δ^{-1} , while the subsequent approach to equilibrium takes place on an extremely slow timescale. This *freezing of the ET dynamics* was never observed in the nonadiabatic regime, but prevails both in the crossover and the adiabatic regime. Below we refer to this novel behavior as “transient ET,” in contrast to the conventional limiting cases of adiabatic and nonadiabatic ET.

Next we increase the value of Δ/ω_c to 2. The numerical results in Fig. 9 reveal a similar picture. Again $k(t)$ fails to exhibit a clear plateau for $T \gtrsim \hbar\Delta/k_B$, but k_{th} can be extracted from $P(t)$. The Marcus formula (14) captures the temperature dependence of k_{th} quite well, see Fig. 7, while the nonadiabatic prediction still reproduces qualitative features, now overestimating the rate by a factor ≈ 1.4 . Adiabatic dynamics [16] already describes the transient dynamics, underlining adiabatic tendencies in the bath, but no oscillations are observed (within error bars). For $T \lesssim 0.6\hbar\Delta/k_B$, $P(t)$ develops a local minimum-maximum pair in the short-time domain $t \lesssim \Delta^{-1}$, whose amplitude increases as $T \rightarrow 0$. For $T \lesssim 0.3\hbar\Delta/k_B$, we again observe transient ET as described above. Apparently, ET dynamics becomes quite

complex in this regime.

C. Adiabatic limit

The transition into the adiabatic regime was studied by increasing Δ/ω_c up to 20 for two temperatures, $T = 10\hbar\Delta/k_B$ and $\hbar\Delta/k_B$. Both $P(t)$ and $k(t)$ are expected to eventually follow the adiabatic prediction [16] for large Δ/ω_c , showing damped oscillations with decreasing amplitude for lower temperatures. These oscillations are not due to electronic coherence but a consequence of “nuclear” (vibrational) coherence. Although adiabatic theory correctly gives $dP/dt(0) = 0$, it is well-known *not* to reproduce the correct long-time dissipative behavior [7]. Nevertheless, for $t \ll \tau_{\text{relax}}$, conventional wisdom expects that it should still provide a useful approximation. The short-time dynamics of both $P(t)$ and $k(t)$ indeed closely follows adiabatic theory. For $T = \hbar\Delta/k_B$, a plateau in $k(t)$ is found, yielding a transfer rate k_{th} that decreases with increasing Δ/ω_c , until oscillations eventually occur at $\Delta/\omega_c \gtrsim 5$. Since (within error bars) $P(t)$ shows no oscillations even for $\Delta/\omega_c = 5$, we can assign a rate to ET under a nonequilibrium initial preparation. Only for larger Δ/ω_c , evidence for oscillations in $P(t)$ can be observed, see also Ref. [59].

Several important differences to adiabatic theory appear in our data, see Figs. 10 and 11. With regard to $k(t)$, the observed oscillations have a smaller amplitude, their mean value is larger, and the oscillation frequency is higher. Adiabatic theory assumes a static bath, which under a dynamical description implies incorrect long-time behavior and overly pronounced oscillations. This qualitatively explains the first two differences. The increase of the oscillation frequency is then due to the larger energy difference between the two adiabatic potential surfaces away from the barrier region, since the region away from the barrier top is probed extensively by a dynamical bath. Turning next to $P(t)$, adiabatic theory fails to reproduce the observed steep descend at the end of the transient dynamics. This can be explained in terms of the bath distribution. In adiabatic theory, the distribution remains centered around the donor state, see Eq. (7), so that there is a low probability of reaching the transition region, and hence too slow ET dynamics is predicted. The improved adiabatic description [16] captures the damping of the oscillation amplitude and the increase of the frequency much more accurately. However, since it is still based on an average over a static bath distribution, it again misses the steep descend of $P(t)$ and the correct mean value for $k(t)$ at times $t > t_{\text{trans}}$. For increasing Δ/ω_c , adiabatic theory then provides a systematically better description, although substantial differences remain even at $\Delta/\omega_c = 20$. For $T = 10\hbar\Delta/k_B$, we get a similar picture, see Fig. 10. However, as expected from our above discussion, $k(t)$ does not exhibit a

plateau. The transition from incoherent to coherent (oscillatory) behavior in $P(t)$ takes place between $\Delta/\omega_c = 5$ and 10. Remarkably, true adiabatic dynamics is realized only for about half an oscillation period, this being virtually independent of Δ/ω_c . This shows that the long-time relaxation process not captured by adiabatic theory sets in much earlier than thought previously.

D. Validity of rate description

Having identified the threshold to the adiabatic regime (at least for $\Lambda = 10\Delta$ and $k_B T/\hbar\Delta = 1, 10$), we next comment on the validity of a rate description for ET. A rate description for $P(t)$ turns out to be appropriate for $\Delta/\omega_c \lesssim 5$, where accurate fits of the numerically exact rates to analytical theory are possible. For small Δ/ω_c , the rate is given by the nonadiabatic prediction (12), while in the crossover regime, the Marcus rate (14) is superior. The Marcus formula assumes a classical bath, and hence becomes more appropriate for large Δ/ω_c , where the bath is very slow and hence classical. Remarkably, the Marcus formula can be made to work even outside the true classical (high-temperature) regime, see Fig. 12. In the high-temperature limit, the solvent frequency ω_r appearing in Eq. (14) is given by Eq. (16). For lower (but not too low) temperatures, the Marcus formula still provides a good estimate for the exact rate within the regime stated above, provided ω_r is taken in the form

$$\omega_r = \frac{\omega_c}{2} \left(\frac{\omega_c}{\Lambda} \right)^{q(T)}. \quad (34)$$

In the high-temperature limit, our data indicate that Eq. (34) reduces to Eq. (16), implying $q(T) \rightarrow 0$ for high temperatures. At low temperatures, however, a positive value for $q(T)$ is found, see Fig. 12. Of course, at sufficiently low temperatures, the quantum-mechanical “transient regime” mentioned above is entered, where the Marcus formula breaks down. Nevertheless, Eq. (34) represents a noticeable improvement over Eq. (16) for a significant range of intermediate temperatures. We term this low-temperature region, where classical Marcus theory along with Eq. (34) becomes accurate, “extended Marcus regime.” That such a regime could indeed exist may be rationalized by noting that for $\Delta/\omega_c \gtrsim 1$, the bath behaves already rather classically, yet quantum fluctuations significantly renormalize the solvent frequency scale ω_r at low-to-intermediate temperatures. It would clearly be interesting to provide an analytical derivation for Eq. (34).

Notably, for $\Delta/\omega_c \gtrsim 10$, no rate description is possible anymore, neither based on $P(t)$ nor on $k(t)$, since ET dynamics is dominated by vibrational coherence. The rate formalism also becomes useless at very low temperatures, $T \lesssim 0.2\hbar\Delta/k_B$, within the crossover regime. As elaborated above, in this “transient regime,” k_{th} is almost zero

such that long-time relaxational ET is essentially frozen in. The important ET dynamics then happens during the initial transient, $t \lesssim \tau_{\text{trans}}$. Here our simulations for $P(t)$ reveal a quite complex behavior. After a very slow initial onset, a fast transient is found, which eventually ends in a local minimum marking the transition to the frozen relaxation regime, $k_{th} \approx 0$. This transient regime does not extend into the nonadiabatic region. For instance, for $T = 0.2\hbar\Delta/k_B$, it could only be observed for $\Delta/\omega_c \gtrsim 0.2$.

V. CONCLUSIONS AND DISCUSSION

Using the spin-boson model as a description for ET processes, we have calculated the thermal transfer rate k_{th} for two different reorganization energies, $\Lambda = 10\Delta$ and $\Lambda = 50\Delta$, where Δ is twice the electronic coupling between the two redox states. Our real-time PIMC simulations are able to cover the full range of temperatures and adiabaticity parameters Δ/ω_c , where ω_c denotes a typical prominent bath frequency. In this paper, we have confined ourselves to symmetric (unbiased) ET systems. The location of the calculated rates in parameter space are schematically shown in Fig. 13. The time-dependent function $k(t)$, see Eq. (9), is a powerful means both to obtain k_{th} and to decide whether a rate description is appropriate in the first place. In the absence of electronic or vibrational coherence, this rate also describes the exponential decay of the electronic population $P(t)$, provided the timescales for transient dynamics τ_{trans} and thermal relaxation τ_{relax} are sufficiently well separated. However, even in the absence of such a separation, $P(t)$ can often be described by a rate with good accuracy. In this case we found that k_{th} can be extracted from $k(t)$ if the transition between transient motion and the relaxation process can be clearly identified, this usually being the case if transient motion displays a pronounced peak. That there exist differences in the ET dynamics obtained from $P(t)$ or $k(t)$ should not come as a surprise, since these quantities correspond to different initial preparations.

In the nonadiabatic regime, Eq. (12) captures the thermal transfer rate accurately for $\Delta/\omega_c \lesssim 0.1$. Even for $\Delta/\omega_c = 1$ or 2, nonadiabatic theory typically overestimates k_{th} by only a small factor of the order 1 to 2, reflecting the increasing relevance of recrossing events neglected in Eq. (12). Based on our simulations, we were also able to give precise bounds for the validity of the so-called scaling picture, see Eq. (32). The crossover to the adiabatic regime is then surprisingly well described by the famous Marcus theory, see Eq. (14). For high temperatures (within the classical regime), the solvent scale ω_r in Eq. (14) is given by Eq. (16). For lower temperatures, we identified an “extended” Marcus regime, where ω_r is empirically given by Eq. (34). Eventually, for very low temperatures, $T \lesssim \hbar\Delta/k_B$, ET dynamics is almost

completely restricted to transient motion, which cannot be explained by Marcus theory but requires a full dynamical description. In this regime, analytical progress is most difficult, and our exact data reveal the presence of a “transient regime,” where ET proceeds solely via this fast initial transient, while long-time relaxation is extremely slow. Finally, we have shown that for $\Delta/\omega_c \gtrsim 10$, ET dynamics is fully coherent, and no rate description is possible. A comparison to the adiabatic description [16] reveals that the latter can only explain the dynamics of both $P(t)$ and $k(t)$ for times up to τ_{trans} .

Our findings are summarized in the schematic “phase diagram” depicted in Fig. 14. Within large areas of parameter space, ET can be described by an exponential decay after a transient timescale, $t > \tau_{\text{trans}}$. Throughout this rate regime, the corresponding rate constant is very well captured by analytical approaches, namely the nonadiabatic approximation for small Δ/ω_c , and Marcus theory for intermediate-to-large Δ/ω_c . However, a breakdown of the rate description can be observed in two different cases. In the strongly adiabatic regime, nuclear (vibrational) coherence causes oscillatory behavior. In addition, at very low temperatures within the crossover regime, relaxation is frozen in, and the transient motion dominates the ET process (“transient regime”).

Clearly, the computational method used in this paper has the potential to solve many other interesting problems via real-time PIMC. In the context of ET dynamics, we have not reported results for the biased system, but plan to do so in the future.

ACKNOWLEDGMENTS

We wish to thank J. Ankerhold, M. Dikovskiy, H. Grabert, A. Lucke, C.H. Mak, and J.T. Stockburger for valuable discussions. Financial support by the Volkswagen-Stiftung (No. I/73 259) is acknowledged.

APPENDIX A: COMPUTATIONAL DETAILS

In this Appendix, some details and improvements over the approach of Ref. [59] are summarized. Paths are blocked together in the following way. The discretized contour γ is divided into L consecutive parts $\{z_1, \dots, z_{q_1}\}, \dots, \{z_{q_{L-1}+1}, \dots, z_N\}$, corresponding to the different levels $l = 1, \dots, L$, dividing the spin paths $\{\sigma_j\}$ into L respective subsets $\{\sigma_j\}_l$. Starting on the first level, for each configuration of the $\{\sigma_j\}_{l>1}$ the respective level-1 block is formed by all possible configurations of the sub-path $\{\sigma_j\}_1$. Switching to the second level, changing only the spins $\{\sigma_j\}_2$ with all others fixed gives a level-2 block for each configuration of the $\{\sigma_j\}_{l>2}$. Clearly, each level-2 block contains a whole set of level-1 blocks. This scheme is continued until on the highest

level L , the final sampling of expectation values is carried out, with strongly reduced sign problem.

To calculate the appropriate block averages, the total action must factorize with respect to the different levels. An appropriate partitioning of $\Phi[\{\bar{\sigma}_m, \eta_j, \xi_j\}]$ is given by

$$\begin{aligned} \Phi_1[\{\bar{\sigma}_m, \eta_j, \xi_j\}] &= \sum_{m=2}^r \bar{\sigma}_m \left[\sum_{n>m}^r Y_{mn} \bar{\sigma}_n \right. \\ &+ \sum_{j=1}^q \xi_j Z_{jm} + \frac{1}{4} \sigma'_1 (L_{2q+m,1} + L_{2q+m,2q+1}) \left. \right] \\ &+ \sum_{k=2}^{q_1} \sum_{j>k}^q \xi_j (\Lambda_{jk} \xi_k + i X_{jk} \eta_k) - \frac{\Lambda_{11}}{4} \sigma'_1 \sigma'_1 \\ &- \frac{\Lambda_{22}}{4} \sum_{j=1}^{q_1} \sigma_j \sigma'_j, \end{aligned}$$

$$\begin{aligned} \Phi_{l>1}[\{\eta_j, \xi_j\}_{l \geq l}] &= \sum_{k=q_{l-1}+1}^{q_l} \sum_{j>k}^q \xi_j (\Lambda_{jk} \xi_k + i X_{jk} \eta_k) \\ &- \frac{\Lambda_{22}}{4} \sum_{j=q_{l-1}+1}^{q_l} \sigma_j \sigma'_j \end{aligned} \quad (\text{A1})$$

(note $\Lambda_{jj} = \Lambda_{22}$ for $2 \leq j \leq q$) with $\Phi[\{\bar{\sigma}_m, \eta_j, \xi_j\}] = \sum_{l=1}^L \Phi_l[\{\bar{\sigma}_m, \eta_j, \xi_j\}_l]$. The contribution from the free propagator is split in the same manner. Here we include the imaginary-time spins into the first level, since they contribute only weakly to the overall sign problem. Therefore they can be assigned to any level of real-time spins without significantly affecting the sign problem. Since the numerical effort to update spins increases for high levels, it saves computing time to put them into the lowest one.

For a computation of $C(t)$, a slight modification of previous MLB formulations is necessary since in Refs. [57–60] averages can be computed only on time slices belonging to the topmost level. This extension of MLB to a computation of an arbitrary n -point function

$$A(t_1, \dots, t_n) = \langle A[\{\sigma_j\}] \rangle \simeq Z^{-1} \sum_{\{\sigma_j\}} A[\{\sigma_j\}] \rho[\{\sigma_j\}] \quad (\text{A2})$$

is described next. At first a dependence of $A(t_1, \dots, t_n)$ on all time slices seems to contradict the philosophy underlying MLB, namely tackling the sign problem by replacing the sampling process over all possible system paths by one over the level- L block only. However, decomposing A in the same way as Φ ,

$$A[\{\sigma_j\}] = \prod_{l=1}^L A_l[\{\sigma_j\}_{l \geq l}], \quad (\text{A3})$$

block averages of A_l for $l < L$ remove all dependence on lower-level spins. Therefore the remaining accumulation process can again be performed by sampling on the highest level only. These block averages are calculated as modified “bonds” $\hat{B}_l[\{\sigma_j\}_{\nu>l}] = A_{l+1}[\{\sigma_j\}_{\nu>l}]B_l[\{\sigma_j\}_{\nu>l}]$ where B_l denotes the “bond” of Ref. [59],

$$B_l[\{\sigma_j\}_{\nu>l}] = C_{l-1}^{-1} \sum_{\{\sigma_j\}_l} B_{l-1}[\{\sigma_j\}_{\nu\geq l}] e^{-W_l(\{\sigma_j\}_{\nu\geq l})} \quad (\text{A4})$$

with the normalization $C_{l-1} = \sum_{\{\sigma_j\}_l} \mathcal{P}_{l-1}[\{\sigma_j\}_l]$ of the weight for level- l bonds,

$$\mathcal{P}_{l-1}[\{\sigma_j\}_l] = \left| B_{l-1}[\{\sigma_j\}_l, \{\sigma_j\}_{l+1}^0, \dots, \{\sigma_j\}_L^0] \times e^{-W_l(\{\sigma_j\}_l, \{\sigma_j\}_{l+1}^0, \dots, \{\sigma_j\}_L^0)} \right|. \quad (\text{A5})$$

Sums run over all possible configuration of level- l spins $\{\sigma_j\}_l$, and $\{\sigma_j^0\}_{\nu<l}$ denotes their initial configuration at the start of the MC trajectory. Hence $A(t_1, \dots, t_n)$ can be written as

$$A(t_1, \dots, t_n) = \frac{\sum_{\{\sigma_j\}_L} \hat{B}_{L-1}[\{\sigma_j\}_L^{(i)}] e^{-W_L[\{\sigma_j\}_L^{(i)}]}}{\sum_{\{\sigma_j\}_L} B_{L-1}[\{\sigma_j\}_L^{(i)}] e^{-W_L[\{\sigma_j\}_L^{(i)}]}} \\ \simeq \frac{\sum_{i=1}^K \frac{\hat{B}_{L-1}[\{\sigma_j\}_L^{(i)}] \exp\{-W_L[\{\sigma_j\}_L^{(i)}]\}}{B_{L-1}[\{\sigma_j\}_L^{(i)}] \exp\{-W_L[\{\sigma_j\}_L^{(i)}]\}}}{\sum_{i=1}^K \frac{B_{L-1}[\{\sigma_j\}_L^{(i)}] \exp\{-W_L[\{\sigma_j\}_L^{(i)}]\}}{B_{L-1}[\{\sigma_j\}_L^{(i)}] \exp\{-W_L[\{\sigma_j\}_L^{(i)}]\}}}, \quad (\text{A6})$$

where the sums in the last expression run over K configurations $\{\sigma_j\}_L^{(i)}$ of the level- L spins distributed according to $\mathcal{P}_L[\{\sigma_j\}_L]$. Here K is the usual MLB sampling number [57], with typical values $K \approx 200$ employed in the simulations. Therefore $A(t_1, \dots, t_n)$ is accessible to a MLB scheme which not only soothes the sign problem due to interfering phase factors of different spin paths, but also takes care of alternating signs of the lower-level contributions to A .

Finally we outline a scheme suitable for compensating for different initial preparations, i.e. computing $P(t)$ with the same MC trajectories as $C(t)$. After discretizing the corresponding path integrals, $P(t)$ can be written as, cp. Eq. (26),

$$P(t) = Z_P^{-1} \sum_{\{\sigma_j\}' } \sigma_{q+1} \rho_P[\{\sigma_j\}'], \\ \rho_P[\{\sigma_j\}'] = K(+1, \sigma_2) K^*(+1, \sigma_2') \left[\prod_{i=2}^N K(\sigma_i, \sigma_{i+1}) \right] \\ \times e^{-\Phi_P[\{\sigma_j\}'] + \zeta[\{\sigma_j\}']}, \quad (\text{A7})$$

where the summation now only includes real-time spins $\sigma(t > 0)$, i.e. $\{\sigma_j\}' = \{\sigma_2, \dots, \sigma_{2q}\}$. The corresponding

influence functional $\Phi_P[\{\sigma_j\}']$ is obtained from Eq. (30) by dropping all terms with imaginary-time spins $\bar{\sigma}_m$ and setting the $t = 0$ spins σ_1, σ_1' to $+1$. In addition

$$\zeta[\{\sigma_j\}'] = i \sum_{j=2}^q \xi_j \text{Im}\{Q((j-1/2)\Delta_j) - Q((j-3/2)\Delta_j)\} \quad (\text{A8})$$

includes a contribution describing the initial preparation of the bath [7,59]. To put $P(t)$ into the form of Eq. (A2), we rewrite Eq. (26) according to

$$P(t) = 2^{-m-2} Z_P^{-1} \sum_{\{\sigma_j\}} \left(\sigma_{q+1} \frac{\rho_P[\{\sigma_j\}']}{\rho[\{\sigma_j\}]} \right) \rho[\{\sigma_j\}], \quad (\text{A9})$$

with [note that $\sum_{\{\sigma_1, \sigma_1'\}} \sum_{\{\bar{\sigma}_m\}} 1 = 2^2 \cdot 2^m$]

$$2^{-m-2} Z_P^{-1} = \left(2^{m+2} \sum_{\{\sigma_j\}'} \rho_P[\{\sigma_j\}'] \right)^{-1} \\ = \left(\sum_{\{\sigma_j\}} \frac{\rho_P[\{\sigma_j\}']}{\rho[\{\sigma_j\}]} \rho[\{\sigma_j\}] \right)^{-1}. \quad (\text{A10})$$

The effect of the different initial preparation is now absorbed by the factor ρ_P/ρ . Consequently $P(t)$ can now be computed as described above with $A[\{\sigma_j\}] = \sigma_{q+1} \rho_P[\{\sigma_j\}']/\rho[\{\sigma_j\}]$. The prefactor can be treated on the same footing. Thus, with the above extension in mind, $P(t)$ can be calculated from the same MC trajectories used for sampling $C(t)$ within our MLB-PIMC approach.

-
- [1] R.A. Marcus, J. Chem. Phys. **24**, 966 (1956).
 - [2] R.A. Marcus and N. Sutin, Biochim. Biophys. Acta **811**, 265 (1985).
 - [3] A.M. Kuznetsov, *Charge transfer in physics, chemistry and biology* (Gordon and Breach, 1995).
 - [4] H. Tributsch and L. Pohlmann, Science **279**, 1891 (1998).
 - [5] D. Chandler, in *Liquids, Freezing and the Glass Transition*, ed. by D. Levesque, J.P. Hansen. and J. Zinn-Justin (Elsevier Science, North Holland, 1991), Les Houches 51, Part 1.
 - [6] X. Song and A.A. Stuchebrukhov, J. Chem. Phys. **99**, 969 (1993).
 - [7] U. Weiss, *Quantum Dissipative Systems*, Series in Modern Condensed Matter Physics, Vol. 2 (World Scientific, Singapore, 1998).
 - [8] R.P. Feynman and F.L. Vernon, Ann. Phys. (N.Y.) **24**, 118 (1963).
 - [9] H. Grabert, P. Schramm, and G.-L. Ingold, Phys. Rep. **168**, 115 (1988).

- [10] G.A. Voth, D. Chandler, and W.H. Miller, *J. Chem. Phys.* **93**, 7009 (1989).
- [11] P. Hänggi, P. Talkner, and M. Borkovec, *Rev. Mod. Phys.* **62**, 251 (1990).
- [12] V.G. Levich, *Adv. Electrochem. Electrochem. Eng.* **4**, 249 (1965).
- [13] A.A. Ovchinnikov and M.Y. Ovchinnikova, *Zh. Eksp. Teor. Fis.* **56**, 1278 (1969) [*Sov. Phys. JETP* **29**, 688 (1970)].
- [14] M.A. Vorotyntsev, R. Dogonadze, and A.M. Kuznetsov, *Dokl. Akad. Nauk SSSR* **195**, 1135 (1970).
- [15] R. Egger, C.H. Mak, and U. Weiss, *J. Chem. Phys.* **100**, 2651 (1994).
- [16] B. Carmeli and D. Chandler, *J. Chem. Phys.* **82**, 3400 (1985); *ibid.* **89**, 452 (1988).
- [17] J.N. Gehlen and D. Chandler, *J. Chem. Phys.* **97**, 4958 (1992).
- [18] A.I. Burshtein and Yu. Georgievskii, *J. Chem. Phys.* **100**, 7319 (1994).
- [19] L. Mühlbacher, A. Lucke, and R. Egger, *J. Chem. Phys.* **110**, 5851 (1999).
- [20] M.J. Hornbach and Yu. Dakhnovskii, *J. Chem. Phys.* **111**, 5073 (1999).
- [21] A. Garg, J.N. Onuchic, and V. Ambegaokar, *J. Chem. Phys.* **83**, 4491 (1985).
- [22] F. Lesage and H. Saleur, *Phys. Rev. Lett.* **80**, 4370 (1998).
- [23] A.J. Leggett, S. Chakravarty, A.T. Dorsey, M.P.A. Fisher, A. Garg, and W. Zwerger, *Rev. Mod. Phys.* **59**, 1 (1987).
- [24] R. Egger, C.H. Mak, and U. Weiss, *Phys. Rev. E* **50**, 655 (1994).
- [25] M. Grifoni, E. Paladino, and U. Weiss, *Eur. Phys. J. B* **10**, 719 (1999).
- [26] R. Silbey and R.A. Harris, *J. Chem. Phys.* **80**, 2615 (1984).
- [27] W.Th. Pollard, A.K. Felts, and R.A. Friesner, *Adv. Chem. Phys.* **93**, 77 (1996).
- [28] G. Stock, *Phys. Rev. E* **51**, 3038 (1995).
- [29] G. Stock, *J. Chem. Phys.* **103**, 1561 (1995).
- [30] G. Stock and M. Thoss, *Phys. Rev. Lett.* **78**, 578 (1997).
- [31] X. Sun, H. Wang, and W.H. Miller, *J. Chem. Phys.* **109**, 7064 (1998).
- [32] H. Wang, X. Song, D. Chandler, and W.H. Miller, *J. Chem. Phys.* **110**, 4828 (1999).
- [33] A. Lucke, J. Stockburger, and C.H. Mak, *J. Chem. Phys.* **111**, 10843 (1999).
- [34] A.A. Golosov, R.A. Friesner, and P. Pechukas, *J. Chem. Phys.* **110**, 138 (1999).
- [35] A.A. Golosov, R.A. Friesner, and P. Pechukas, *J. Chem. Phys.* **112**, 2095 (2000).
- [36] J. Casado-Pascual, C. Denk, M. Morillo, and R.I. Cukier, *J. Chem. Phys.* **113**, 11176 (2000).
- [37] H. Wang, M. Thoss, and W.H. Miller, *J. Chem. Phys.* **115**, 2979 (2001); M. Thoss, H. Wang, and W.H. Miller, *J. Chem. Phys.* **115**, 2991 (2001).
- [38] H. Wang, *J. Chem. Phys.* **113**, 9948 (2000).
- [39] N. Makri and D.E. Makarov, *J. Chem. Phys.* **102**, 4600 (1995).
- [40] M. Winterstetter and W. Domcke, *Chem. Phys. Lett.* **236**, 445 (1995).
- [41] J. Stockburger and C.H. Mak, *Phys. Rev. Lett.* **80**, 2657 (1998).
- [42] J. Stockburger and H. Grabert, *Phys. Rev. Lett.* **88**, 170407 (2002).
- [43] T.A. Costi and C. Kieffer, *Phys. Rev. Lett.* **76**, 1683 (1996).
- [44] T.A. Costi, *Phys. Rev. Lett.* **80**, 1038 (1998).
- [45] M. Keil and H. Schoeller, *Phys. Rev. B* **63**, 180302 (2001).
- [46] *Quantum Monte Carlo Methods in Condensed Matter Physics*, ed. by M. Suzuki (World Scientific, Singapore, 1993), and references therein.
- [47] See, for instance, E.Y. Loh Jr., J. Gubernatis, R.T. Scalettar, S.R. White, D.J. Scalapino, and R.L. Sugar, *Phys. Rev. B* **41**, 9301 (1990).
- [48] S. Chakravarty and J. Rudnick, *Phys. Rev. Lett.* **75**, 501 (1995).
- [49] K. Völker, *Phys. Rev. B* **58**, 1862 (1998).
- [50] D. Bailey, M. Hurley, and H.K. McDowell, *J. Chem. Phys.* **109**, 8262 (1998).
- [51] E.C. Behrman and P.G. Wolynes, *J. Chem. Phys.* **83**, 5863 (1985).
- [52] C.H. Mak and D. Chandler, *Phys. Rev. A* **44**, 2352 (1991).
- [53] R. Egger and C.H. Mak, *Phys. Rev. B* **50**, 15210 (1994).
- [54] V.S. Filinov, *Nucl. Phys. B* **271**, 717 (1986).
- [55] J.D. Doll, T.L. Beck, and D.L. Freeman, *J. Chem. Phys.* **89**, 5753 (1988).
- [56] C.H. Mak and R. Egger, *Adv. Chem. Phys.* **93**, 39 (1996), and references therein.
- [57] C.H. Mak, R. Egger, and H. Weber-Gottschick, *Phys. Rev. Lett.* **81**, 4533 (1998).
- [58] C.H. Mak and R. Egger, *J. Chem. Phys.* **110**, 12 (1999).
- [59] R. Egger, L. Mühlbacher, and C.H. Mak, *Phys. Rev. E* **61**, 5961 (2000).
- [60] M. Dikovsky and C.H. Mak, *Phys. Rev. B* **63**, 235105 (2001).
- [61] We consider only $\alpha \geq 1/2$. ET dynamics is normally incoherent with respect to electronic motion, while for $\alpha < 1/2$, spin-boson dynamics shows electronic coherence [7].

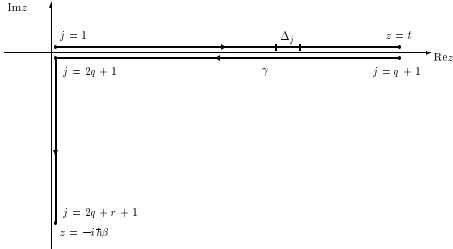


FIG. 1. Kadanoff-Baym contour γ in the complex-time plane and a possible discretization.

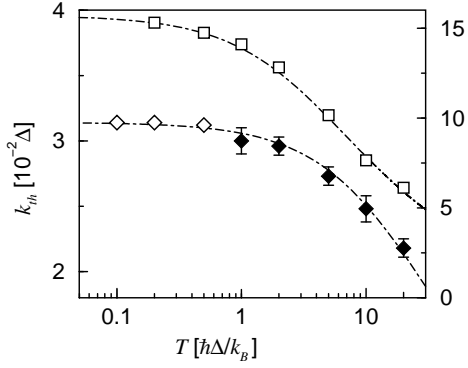


FIG. 2. Thermal transfer rate k_{th} for $\alpha = 1/2$, $\omega_c = 50\Delta$ (diamonds, left axis) and $\omega_c = 10\Delta$ (squares, right axis). Filled symbols refer to values obtained from $k(t)$, open ones to those obtained from $P(t)$. Vertical lines indicate error bars from statistical sampling uncertainties. The error in fitting $P(t)$ to an exponential decay is of the order of the symbol size. The dashed-dotted curves represent the nonadiabatic result (20).

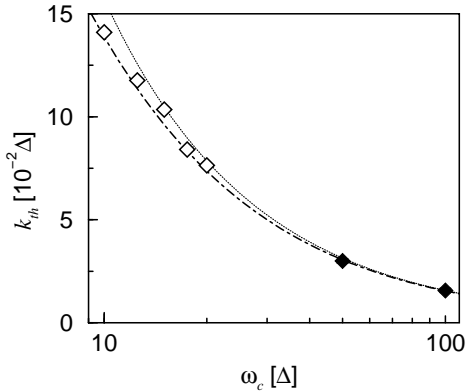


FIG. 3. Same as Fig. 2 but as a function of ω_c/Δ for fixed $T = \hbar\Delta/k_B$. The dotted curve denotes the rate according to the scaling limit, while the dashed-dotted one gives Eq. (20).

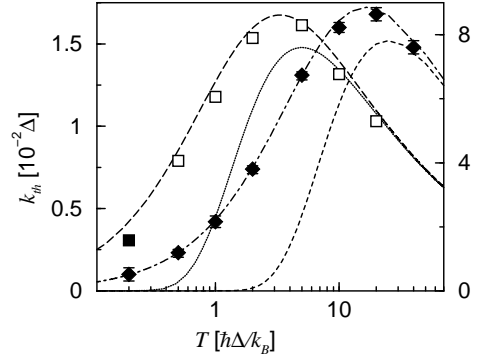


FIG. 4. Thermal transfer rate k_{th} for $\alpha = 1$ with $\Lambda = 50\Delta$ (diamonds, left axis) and $\Lambda = 10\Delta$ (squares, right axis). The curves give Eq. (21).

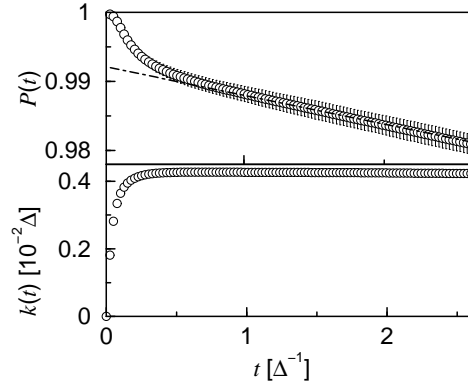


FIG. 5. $P(t)$ and $k(t)$ for $\omega_c/\Delta = 25$, $\Lambda = 50\Delta$, and $T = \hbar\Delta/k_B$. The dashed-dotted line represents $\exp(-0.0042\Delta t) - 0.008$, in agreement with the plateau value of $k(t)$.

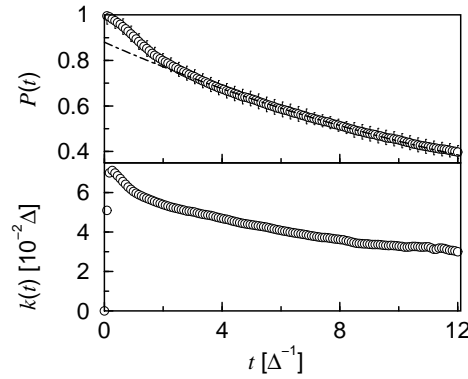


FIG. 6. Same as Fig. 5 but for $\Lambda = 10\Delta$, $\Delta/\omega_c = 1$, and $T = 3.333\hbar\Delta/k_B$. The dashed-dotted line represents $\exp(-0.057\Delta t) - 0.12$.

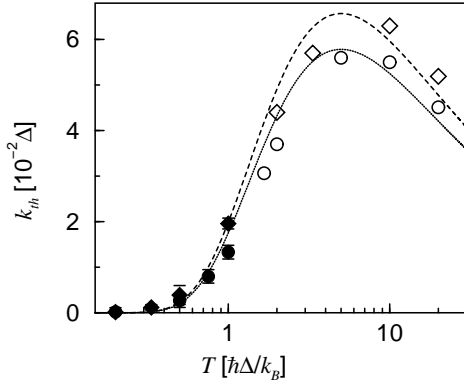


FIG. 7. ET rate k_{th} for $\Lambda = 10\Delta$, with $\omega_c = \Delta$ (diamonds) and $\omega_c = 0.5\Delta$ (circles). The dashed and solid curves represent the corresponding Marcus rates (14) with $\omega_r = \omega_c/2$.

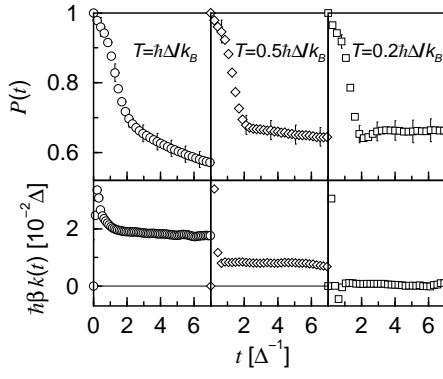


FIG. 8. Same as Fig. 6 but for lower temperatures. Data for $T = 0.1\hbar\Delta/k_B$ (not shown) are virtually identical to those for $T = 0.2\hbar\Delta/k_B$, indicating that the zero-temperature limit has been reached.

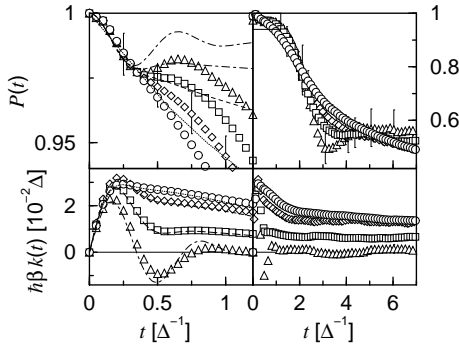


FIG. 9. Same as Fig. 8, but for $\Delta/\omega_c = 2$, $T = 2\hbar\Delta/k_B$ (circles), $T = \hbar\Delta/k_B$ (diamonds), $T = 0.6\hbar\Delta/k_B$ (squares) and $T = 0.2\hbar\Delta/k_B$ (triangles). The left side of the graph shows the initial transient dynamics. The box in the top left corner of the upper right graph represents the corresponding scale of the upper left graph. The dotted [dashed, long dashed, dot-dashed] curve represents the adiabatic approximation for $T = 2\hbar\Delta/k_B$ [$\hbar\Delta/k_B$, $0.6\hbar\Delta/k_B$, $0.2\hbar\Delta/k_B$].

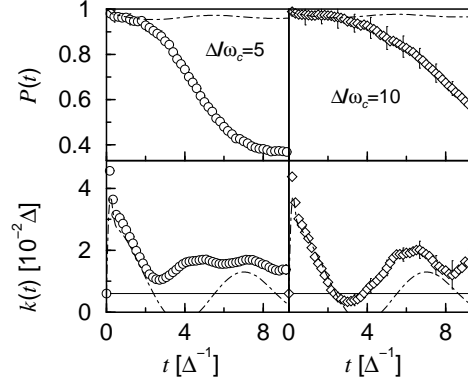


FIG. 10. $P(t)$ and $k(t)$ for $T = \hbar\Delta/k_B$, $\Delta/\omega_c = 5$ (left) and $\Delta/\omega_c = 10$ (right). Dot-dashed curves represent the adiabatic prediction.

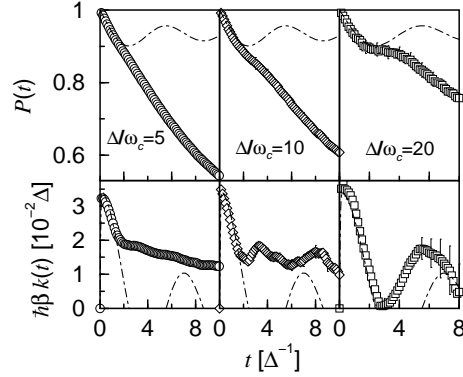


FIG. 11. Same as Fig. 10, but for $T = 10\hbar\Delta/k_B$ and (from left to right) $\Delta/\omega_c = 5, 10$ and 20 .

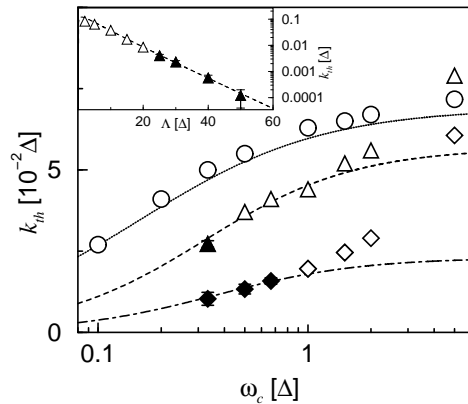


FIG. 12. Thermal transfer rate k_{th} as a function of ω_c for $T = 10\hbar\Delta/k_B$ (circles), $T = 2\hbar\Delta/k_B$ (triangles) and $T = \hbar\Delta/k_B$ (diamonds). The dotted [dashed, dashed-dotted] lines refer to the Marcus rate with ω_r according to Eq. (34) and $q(T = 10\hbar\Delta/k_B) = 0.0002$ [$q(T = 2\hbar\Delta/k_B) = 0.21$, $q(T = \hbar\Delta/k_B) = 0.26$]. The exact rates exceed the nonadiabatic (maximum) Marcus rate for $\omega_c \gtrsim 5\Delta$ [2Δ , 1.5Δ]. The inset shows k_{th} at $T = 2\hbar\Delta/k_B$ and $\omega_c = 0.5\Delta$ as a function of the reorganization energy Λ , where the dashed curve corresponds to the main graph.

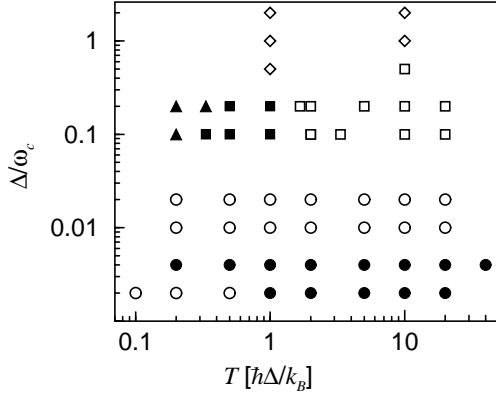


FIG. 13. Location of parameter values where simulations have been carried out. The reorganization energies are $\Lambda = 50\Delta$ for $\Delta/\omega_c = 0.02, 0.04$, and $\Lambda = 10\Delta$ otherwise. Results following the nonadiabatic prediction (12) are denoted by circles, those following the (classical or extended) Marcus formula (14) by squares. Transient behavior is marked by triangles, and oscillatory (adiabatic) dynamics by diamonds.

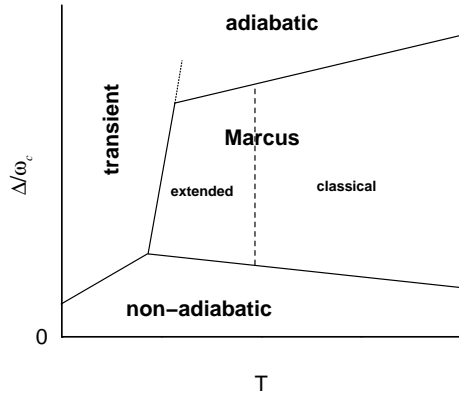


FIG. 14. Schematic ET dynamics “phase diagram.” To obtain quantitative numbers for the crossover lines, refer to Fig. 13.